Research Square

Preprints are preliminary reports that have not undergone peer review.
They should not be considered conclusive, used to inform clinical practice,
or referenced by the media as validated information.

# Passive seismic imaging of the orthomagmatic ore deposits using regional earthquake interferometry: a case study of the Akanvaara V-Cr-PGE deposit in Northern Finland

**Nikita Afonin**

nikita.afonin@gtk.fi

University of Oulu

**Elena Kozlovskaya**

University of Oulu

**Kari Moisio**

University of Oulu

**Shenghong Yang**

University of Oulu

**Jouni Sarala**

University of Oulu

**Research Article**

**Keywords:** passive seismic imaging, regional earthquake interferometry, critical raw materials, cost-effective methods, mineral exploration

**Posted Date:** March 16th, 2026

**DOI:** https://doi.org/10.21203/rs.3.rs-9009391/v1

**License:** This work is licensed under a Creative Commons Attribution 4.0 International License.
Read Full License

**Additional Declarations:** No competing interests reported.

# Passive seismic imaging of the orthomagmatic ore deposits using regional earthquake interferometry: a case study of the Akanvaara V-Cr-PGE deposit in Northern Finland.

Nikita Afonin[1,2], Elena Kozlovskaya[1], Kari Moisio[1], Shenghong Yang[1], Jouni Sarala[1]

[1]University of Oulu, Oulu, Finland
[2]Geological Survey of Finland, Espoo, Finland

*Correspondence to*: Nikita Afonin (nikita.afonin@oulu.fi)

**Abstract.** This paper presents a method for studying the structure of the subsurface in hard rock terrains by interferometry of the Pn-wave coda of the regional seismic events. Using theoretical background and application examples of the teleseismic coda wave interferometry and the teleseismic receiver function methods, we developed data processing and interpretation schemes that convert the Pn coda, recorded in local high resolution passive seismic experiments, into body wave part of the empirical Green's tensor (EGT), i.e. an impulse response of the medium to a virtual seismic source placed either on the ground surface or underground. Based on the general theoretical considerations, we assume that the different components of the EGT evaluated from the Pn coda include body wave arrivals which are reflected and converted on the structural boundaries having different elastic properties. The algorithm was tested with real data recorded within high-resolution passive seismic experiments with 771 three-component seismic instruments in the "Volfram-Chrome-Platinum Group Elements" (V-Cr-PGE) orthomagmatic deposit of the Akanvaara ultramafic intrusion in Northern Finland. From the evaluated EGT it was possible to identify numerous signatures of converted and reflected waves. To interpret these arrivals, we conducted a numerical simulation of a plane wave interaction with a synthetic model of the deposit and found that the arrivals correlate not only with the known structural features of the deposit, but with unknown ones as well. Our study shows that interferometry of the regional Pn-wave coda can be an effective tool for mineral exploration both in greenfield and brownfield cases.

*Keywords:* passive seismic imaging, regional earthquake interferometry, critical raw materials, cost-effective methods, mineral exploration

## 1 Introduction

Knowledge about mechanical properties and structural features of the near-surface part of the geological environment is important in such applications as geotechnical site investigations and monitoring, mineral exploration, geo-energy projects, and seismic hazard assessment. Although it's possible to obtain the solution with controlled source seismic (CSS) methods (reflected, refracted seismic or MASW), it is still a relatively expensive and not always most environmentally friendly approach. Moreover, the application of ground surface CSS methods is challenging in some applications, like the detection of mineralisation zones in ore deposits that are confined to relatively thin inclined layers (Bohlen et al., 2003; Malehmir et al., 2012b). These could be investigated with vertical seismic profiling (e.g. Greenhalgh et al., 2003), in which the waves converted at sub-vertical boundaries can be detected. Nevertheless, this is also quite expensive and non-environmentally friendly method as its implementation requires drilling and the use of active seismic sources, typically explosives.

Demand for critical raw materials requires cost-effective and environmentally friendly methods for example to the exploration of orthomagmatic mineral systems, which include mafic layered intrusions and conduit-type sulphide deposits. These deposits host such critical raw materials (CRM) as platinum-group metals (PGM), nickel (Ni), cobalt (Co), vanadium (V), copper (Cu), which are irreplaceable for a wide set of EU strategic sectors such as aerospace, digital industry, and defence sectors (The European Commission, 2023).

In this study, with passive seismic methods we try to resolve these challenges related to studying the inner structure of orthomagmatic mineral systems. Compared to CSS, passive seismic methods are considered more environmentally friendly, as no artificial seismic energy sources are needed, such as blasts or vibrators. One of

these methods is based on the recording and processing of ambient seismic noise and extracting arrivals of surface and body waves from the calculated Empirical Green's Functions (EGFs) (e.g. Afonin, 2022; Draganov et al., 2009; Oren & Nowack, 2016; Poli et al., 2013). These methods can be an effective solution for some applications when strong ambient noise sources exist near and around the study area like for example industrial plants, mines and roads. Successful applications are known from several experiments in urban areas (e.g. Zhang et. al., 2019; Afonin et. al., 2022; Yang & Shragge, 2023; Sun et. al., 2024). In remote and seismically quiet areas, this method requires special algorithms to improve the quality of EGFs (e.g. Afonin et al., 2019). Nevertheless, results of the studies done in remote and quiet areas of Northern Finland demonstrated that this technique only allows retrieving the surface wave part of the EGFs (Afonin et al., 2021). Relatively low resolution of the results obtained by the surface wave analysis does not allow us to analyze targets where higher resolution would be required, like the delineation of zones associated with mineralisations in ore deposits or the inner structure of mafic layered intrusions. In this study we address this problem with the regional earthquake interferometry which is a passive seismic method based on the analysis of the coda of the regional seismic events.

During the past decade, several passive seismic methods related to the analysis of seismic coda have been developed. Usually, such methods use teleseismic earthquakes. The most popular among these methods are the receiver function methods originally proposed by Vinnik (1977) and teleseismic coda wave interferometry (e.g. Sneider, 2006; Sherbaum, 1987; Wang et al., 2020; Schuster, 2008; Campillo and Paul, 2003). These methods have been used to study the deep structure of the Earth's crust and the upper mantle because of the low-frequency content of the used signal. However, such frequencies are too low for the investigation of the near-surface structures as is done in mineral exploration.

In this study, we utilise the theoretical background and principles of the receiver function method, the passive seismic coda wave interferometry, and the controlled source seismic exploration to develop a passive seismic method for studying the shallow subsurface structures. We tested the data processing algorithm on the real data, recorded in a passive seismic experiment on the Akanvaara Cr-V-PGE deposit in Northern Finland. In the next chapters, we present the theoretical background, method description, as well as details of the synthetic tests and processing of seismic data, and possible applications of the method in mineral exploration tasks in hard rock terrains.

## 2. Theoretical background

The coda wave seismic imaging has significant differences compared to CSS reflection experiments. First, it deals with the forward-scattered waves from the distant sources, not with backscattered waves from the surface sources. Second, in reflection seismic, source position, source wavelet and start time are controlled, but in coda wave imaging, we cannot simply estimate the source wavelet nor its accurate location. Thus, instead of the acoustic approximation of the elastic wave equation used in reflection seismic, we have to consider the full elastic wave equation (Aki & Richards, 2002):

$$\frac{\partial}{\partial x_j}\left(c_{ijkl}\frac{\partial u_k}{\partial x_l}\right) + \rho\frac{\partial^2 u_i}{\partial t^2} = f_i, \quad (1)$$

where $u_k$ is the displacement at a point, $c_{ijkl}$ is the elasticity tensor, ρ is density and $f_i$ is the source term.

Mathematically, the coda wave imaging problem can be formulated as follows (Pavlis, 2005). Assuming that $N_s$ seismic events were recorded by an array of $N_r$ seismic recorders, placed on the Earth's surface at the top of volume V, the task is to estimate one or more physical properties of the medium inside volume V at every point

X of this volume, using three-component seismograms $\boldsymbol{u}_{ij}(\boldsymbol{r}_i, \boldsymbol{s}_j, t)$, where $\boldsymbol{r}_i$ are receiver locations and $\boldsymbol{s}_j$ are source locations and t is time.

All direct imaging techniques are based on single-scattered theory (Stolt & Weiglein, 1985) and Born approximation from perturbation theory (e.g. Aki & Richards, 2002; Wu & Aki, 1985). The starting point in this approximation is that physical properties of the elastic medium (density $\rho$ and elasticity tensor $c_{ijkl}$) are presented as a sum of the reference of the property and its perturbation:

$$\rho = \rho_0 + \delta\rho, \ c_{ijkl} = (c_{ijkl})_0 + \delta c_{ijkl} \tag{2}$$

where 0 denotes the background property and $\delta$ means perturbation.

In the Born series, the zeroth-order term means incident wavefield, and the first-order term defines components of the wavefield that have been scattered once (i.e., the first-order term represents primary reflections and conversions). Higher-order terms represent multiple scattered waves (Weiglein et al., 1997).

Assuming that we can compute Green's function $G_{ij}$ in the reference medium, it has been shown that the scattered wavefield can be computed as (Beylkin & Burridge, 1990):

$$U_{jk}(s, \tau; r, t) = -\iiint \delta\rho \frac{\partial}{\partial t^2}\left(G_{jl} * G_{kl}\right) + \delta c_{lmpq}\left(G_{jp,q} * G_{kl,m}\right)dV \tag{3}$$

where $U_{jk}$ is the k-th component of the scattered wavefield created by virtual point forces in the j direction, created by material property perturbations that scatter the incident wavefield. The scattered wavefield components in an observed seismogram can be obtained by summation over j. Equation (3) is a general description of the single-scattering approximation in an elastic medium.

Thus, the total observed wavefield $\boldsymbol{u}$ can be presented as a superposition of the incident $\boldsymbol{g_0}$ and scattered $\boldsymbol{u_{sc}}$ wavefields:

$$\boldsymbol{u}(\boldsymbol{r}, t) = \boldsymbol{g_0} + \boldsymbol{u_{sc}} \tag{4}$$

In seismology, this scattered wavefield $\boldsymbol{u_{sc}}$ is called coda, which makes up the late part of a seismic signal (Campillo & Paul, 2008). Considering vertically incident P-wave and that multiple scattering plays a prominent part in the seismic coda, the coda of P-wave $\boldsymbol{u_{sc}}$ will contain reflected and transmitted waves and their multiples, which originated on local heterogeneities. The diffusive character of the coda has been revealed by investigating the property of mode equipartition (Weaver, 1982). As shown by Lobkis & Weaver (2008), the coherence of the diffused wavefield can be used to retrieve the Empirical Green's Tensor (EGT). Therefore, the cross-correlation functions of the seismic coda can be calculated between the recordings of all possible channel's pairs of the three-component seismic sensor to obtain all the nine components of the EGT. Assuming that three components of P-wave coda were recorded in Z,R,T coordinate system, where Z means vertical displacement, R radial and T transverse, we denote the recorded coda ground displacement as $\boldsymbol{u_{sc}} = (u_{sc}^Z, u_{sc}^R, u_{sc}^T)$. In this case, the body wave part of the EGT will be:

$$\boldsymbol{G} = \begin{pmatrix} G_{ZZ} & G_{ZR} & G_{ZT} \\ G_{RZ} & G_{RR} & G_{RT} \\ G_{TZ} & G_{TR} & G_{TT} \end{pmatrix}, \tag{5}$$

were $G_{ij} = u_{sc}^i \otimes u_{sc}^j$; $\otimes$ means cross-correlation; i and j correspond to directions Z, R and T.

As was shown by Shuster (2008) in the case when the incident wavefield arrives near-vertically to the ground surface, the diagonal components of the tensor will contain reflected and multiple reflected arrivals of the P and SH waves. At the same time, the non-diagonal components of the tensor will contain a time lag between the direct and the transmitted arrivals (converted PS or SP) from local heterogeneities.

Assuming that P-wave and S-wave velocities are constant above the conversion boundary, one can calculate the depth to the physical boundary, from which the converted PS or SP wave originate. For this the equation proposed for teleseismic P-wave receiver functions by Zhu and Kanamori (2000) can be used:

$$H = \frac{t_{ps}}{\sqrt{\frac{1}{V_S^2} - p^2} - \sqrt{\frac{1}{V_P^2} - p^2}}\ , \tag{6}$$

where $p$ is the ray parameter of the incident P-wave; $t_{ps}$ is the time lag between direct P and converted PS waves; $V_P$ and $V_S$ are P- and S- waves velocities above a conversion boundary.

When the epicentral distances of the seismic events are large compared to the size of a recording array and considering normalization that results from the correlation procedure (Bostock, 2004), we can neglect the ray parameter and assume it is equal to zero. Therefore, Eq. (6) can be simplified:

$$H = (V_P - V_S)t_{ps}. \tag{7}$$

where $t_{ps}$ is a time lag on the non-diagonal components of the EGT, which corresponds to the time lag between the direct P and the converted PS wave originating on the same boundary. This shows that the time delay between direct and converted waves depends on both Vp and Vs and on the time lag.

**3 Method**

The theoretical background described above was developed for studying the deeper parts of the Earth's interior using the coda of teleseismic earthquakes and assuming the Earth's structure is a set of homogeneous horizontal layers beneath a single seismic station (Shuster, 2008). In the mineral exploration applications, we deal with local-scale high-resolution seismic experiments, conducted above mineral systems that are typically characterized by strongly heterogeneous internal structure which cannot be always approximated by a set of homogeneous layers. Although the coda of teleseismic events can be used to obtain general information about the deep structure of mineral systems (namely the Moho depth, existence of magma reservoirs), for exploration tasks a higher resolution is typically required. For this purpose, it is reasonable to consider the Pn coda of the regional and local seismic events as input data, because the frequencies of signals produced by such events are significantly higher than those produced by teleseismic events. At some distances from the epicenter, the Pn-wave arriving at the seismic station can be considered as a vertically arriving plane wave propagating in the medium from the ground surface down to the Moho boundary. For example, in mineral exploration applications in Fennoscandia, where crustal thickness can be as high as 60 km, the Pn-wave can be considered as vertically arriving when epicentral distances are larger than approximately 250 km (Janik et al., 2007, 2009). This upcoming Pn-wave is scattered at upper crustal heterogeneities, that is, in the region from the surface down to several km, producing the Pn-wave coda. Higher frequencies of the Pn-waves compared to the teleseismic P-waves would allow to delineate heterogeneities of relatively small sizes (e.g. features related to the inner structure of layered mafic intrusions or mineralised zones of ore deposits) at depths of a few km.

As was discussed by Shuster (2008), using this method for interferometric imaging of the near subsurface is difficult because of the complex structure of the subsurface and as a result, significant scattering of the upcoming signal. The multiple scattering causes the origin of multiple (higher-order) scattered waves. This can make it difficult to detect the first-order reflected and converted arrivals in the body wave part of the EGT components. To overcome this issue, we need to include a procedure into the data processing workflow to suppress the impact of higher-order scattered waves. For this, the following statements need to be considered:

1. The higher-order scattered arrivals have lower amplitudes and, as a result, attenuate faster than the first-order ones.
2. The first-order scattered waves may originate not only on horizontal boundaries but also on inclined ones.
3. In contrast to the assumptions made for teleseismic coda wave interferometry, the medium cannot be considered as a set of horizontal homogeneous layers. Therefore, the higher-order scattered waves may originate not only on boundaries, but on discontinuities or the heterogeneities within the layers and then propagate in random directions.

Following these, we can assume that the higher-order scattered waves are presented in the coda as uncorrelated noise and, as a result, they should be invisible in the EGT components. Considering that the first-order scattered waves may arrive at non-vertical incidence angles, it is reasonable to convert ZRT components to LQR as in the receiver functions method (Vinnik, 1977) by rotating ZRT seismograms to the incidence angle, which in our case can be estimated by polarisation analysis of early Pn-wave coda (Flinn, 1965; Jurkevics, 1988; Vidale, 1986).
Objective is to detect P-SH, SH-P converted arrivals and reflected P and S waves, thus we should suppress the P waves on QR components and the SH waves on L components, respectively, as well as the ground-roll (local seismic noise) and the effect of higher-order scattered waves. A simple deconvolution, used in the receiver function method (Vinnik, 1977), of the L component from Q and R components cannot be used because this deconvolution can solve only one part of the problem. Based on similarly with optics, where a polarisation filter transmits light that vibrates in one direction while absorbing the light that vibrates in a perpendicular direction, we can apply similar polarisation filter to the seismograms. This procedure can partially remove ground-roll and the impact of higher-order scattered waves and additionally act similarly as deconvolution in the receiver function method.
As was shown by Nguyen (1989), the polarisation filter can be constructed by tracking the trajectories of particle motions. Characteristics of particle motion at a point with their direction of propagation in space make it possible to separate regular waves with different polarisations, propagating in different directions and with different velocities.
To suppress the effect of ground roll, it is reasonable to use the degree of rectilinearity L as proposed by Nguyen (1989):

$$L = 1 - \left(\frac{\lambda_2+\lambda_3}{\lambda_1}\right)^n, \tag{8}$$

where $\lambda_1, \lambda_2, \lambda_3$ are the eigenvalues of the covariance matrix. For Rayleigh waves $L \geq 0.5$ (for more details, see Nguyen, 1989).
Considering this, one can construct the filter as

$$R_L(t) = L^J(\tau),$$

where $\tau = [t_0, t_1], t \in [t_0, t_1]$, is a time window for calculating the covariance matrix; $J$ is a weight, which should be selected depending on how strong Rayleigh waves should be suppressed. The efficiency of such a filter was demonstrated in earlier studies (e.g. Jurkevics, 1988; Brinkman et. al., 2023)
To remove the impact of S waves on the L-component and P waves on the Q and R components, we use a filter, based on the horizontal-to-vertical ratio of displacements in the time domain:

$$P^{ij}(t) = \begin{cases} \dfrac{|u^i_{sc}(t)|}{|\boldsymbol{u}_{sc}(t)|}, E^i_{sc}(t) < E^j_{sc}(t) \\ \dfrac{|u^j_{sc}(t)|}{|\boldsymbol{u}_{sc}(t)|} + 1, E^i_{sc}(t) \geq E^j_{sc}(t) \end{cases}$$

where $\boldsymbol{u}_{sc}(t)$ – vector of full displacement; $E_{sc}^{i}(t)$ – energy on the corresponding channel, calculated as:

$$E_{sc}(t) = \int_{t0}^{t1} u_{sc}^{2}(t)dt, \tag{9}$$

The window length $|t_1 - t_2|$ should be selected reasonably for the analysed signals, taking into account frequency as described above.

Therefore, to obtain filtered seismograms $u_f^i(t)$, we should multiply the initial one, prefiltered by a bandpass filter, $u_{sc}^i(t)$ with both filters:

$$u_f^i(t) = u_{sc}^i(t)P^{ij}(t)R_L(t) \tag{10}$$

## 4 Experimental data

### 4.1 Study site

To test the proposed method, we conducted a passive seismic experiment in the Cr-V-PGE deposit located in the Akanvaara intrusion (Fig. 1).

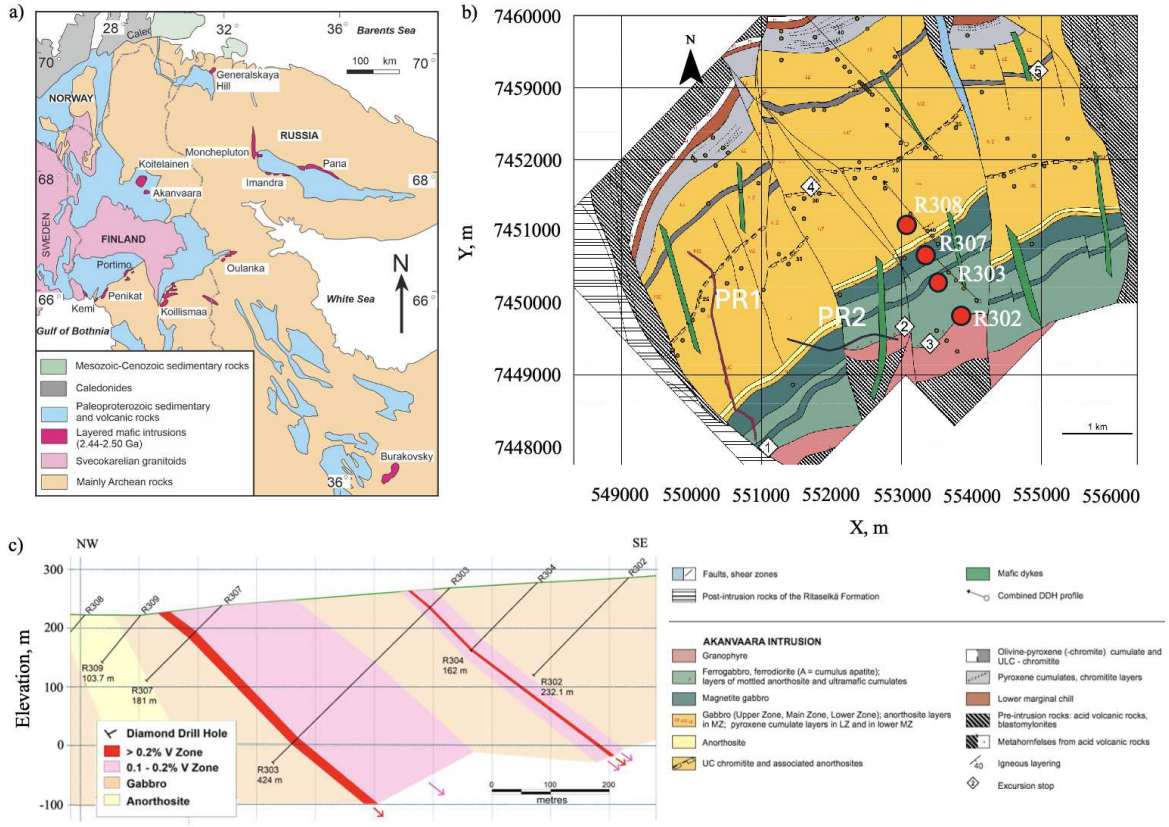



**Fig. 1** Study area: a) on geological map of Finland; b) seismic profiles on the Geological map of Akanvaara (Mutanen, 2005); red circles are drillholes; PR1, PR2 are passive seismic profiles 1 and 2; (coordinate system is ETRS 1989 TM35FIN NE. X axis means East direction, Y axis means North direction); c) geological cross-section (adopted with modifications from Lutynski (2019).

The Akanvaara intrusion is a block-faulted mafic layered intrusion, located in Northern Finland (Fig.1a). It has a monoclinic structure dipping to SE at angles of 25–40° (Fig. 1c). This intrusion was extensively studied by the Geological Survey of Finland (GTK) during the 1990's, when more than 100 diamond drill holes were drilled with comprehensive geochemical analyses across the whole stratigraphy. It consisted of different layers with different compositions below the experiment area. Based on drilling data, Mutanen (1997) and Hanski et al. (2001)

identified three major zones inside the 3.1 km thick part of the intrusion, namely, Lower, Middle and Upper Zones, with thicknesses of approximately 640, 570 and 1900 m, respectively. The Lower Zone (LZ) is mainly composed of pyroxenite with minor olivine-bearing rocks, and the Middle Zone (MZ) contains noritic rocks and anorthosite, and towards gabbroic rocks, magnetite gabbros and ferrogabbros in the Upper Zone (UZ). Multiple layers with elevated PGE contents occur in the LZ and MZ with very minor amount of sulphide are confined to layers of anorthosites on the contact with magnetite gabbro (10s of meters) and V mineralsation is found within thick layers of magnetite gabbro (>100 meters) in the UZ that contain significant amount (up to 30%) of magnetite. The Cr mineralisation is confined to chromitite mineralised layers with thickness of 1-2 meters) distributed inside a thick ultramafic strata (mainly pyroxenites) layers in the LZ and MZ. According to Mutanen (2005), at least 23 chromitite layers have been identified there with thicknesses from several centimetres to several meters. One important potential resource with vanadium mineralisation is the magnetite gabbro occurring in the UZ with a thickness of several hundred meters. The mineralised zones have lengths of approximately 6.5 km along strike (Fig. 1b). As detected in drillcore data (Fig. 1), the upper boundary of the magnetite gabbro is confined to the contact with granophyre.

Assuming exploration with a seismic method, we can define the following targets that may have a contrast of elastic properties with surrounding rocks: a) boundaries of magnetite gabbro strata with V mineralisation; b) boundaries of ultramafic strata with chromitite mineralisation; c) anorthozite layers, which may contain elevated PGE content.

Considering that mineralisation zones inside the Akanvaara layered intrusion are presented as inclined thin layers, we assumed that the Pn-wave coda, recorded above such mineralisation zones, should include PS and SP waves converted on these thin layers. These converted arrivals should be visible in the non-diagonal EGT components. We decided to acquire the data along two high-resolution passive seismic profiles with lengths of 2800 m and 1550 m, respectively. These profiles cross several mineralisation zones of Cr and V in the Akanvaara intrusion (Fig. 1 b,c).

**4.2 Passive seismic experiments and data**

In the first profile (PR 1 in Fig. 1b), 606 GSB-3 seismic recorders with 5 Hz three-component seismic sensors were installed (Geospace Technologies Ltd). These devices recorded seismic data continuously from 2.11.2023 to 9.12.2023. The second part of the experiment was conducted in autumn 2024 (Profile 2, marked as PR 2 in Fig. 1b). In the second profile, in total 165 seismic instruments were used. From these instruments, 72 was three-component autonomous seismic recorders IGU-16HR 3C 2Hz (SmartSolo Inc) and remaining 48 and 45 were GSX's and GSB-3's, respectively (Geospace Technologies Ltd). These recorded seismic data continuously from 28.08 to 2.10 2024. In both cases, we installed instruments alongside roads with a 5 m spacing between sensors. The in-line components of sensors in the first case and cross-line components in the second case were oriented to the NS direction. Devices were provided by the Finnish FLEX-EPOS seismic instrument pool (Hillers et al., 2025).

Previous results of wide-angle reflection and refraction profiles in northern Finland and modelling of propagation of body waves in the crust (Janik et al., 2009; Tiira et al., 2014) demonstrated that the first arrivals of body waves of local and regional seismic events recorded at distances exceeding 250 km are the Pn and Sn phases. These are refracting in the uppermost mantle beneath the Moho boundary and arriving at sub-vertical incident angles to

seismic stations. The online seismic bulletin by the Institute of Seismology of the University of Helsinki (https://www.helsinki.fi/en/institute-seismology) was used to compile a list of 279 (Profile 1) and 917 (Profile 2) seismic events (both earthquakes and mining blasts) for our experiment times. The selected seismic events were mainly production blasts in the quarries of the Kola Peninsula, Sweden and Southern Finland (Fig. 2). These events had magnitudes larger than one and epicentral distances between 250 – 800 km from the study area. In this case, the coda of Pn and Sn should contain the secondary arrivals of P and S waves, including the waves converted at intracrustal boundaries. As the wavelengths of Pn and Sn waves are hundreds of meters and their incidence angles are sub-vertical, these can be considered as plane waves for the seismic arrays with sensor distances smaller than the wavelengths. This assumption justifies the application of converted wave detection by stacking recordings of multiple events located at different azimuths, and utilising similar interpretation techniques as proposed in the receiver function techniques (Vinnik, 1977, 2019).

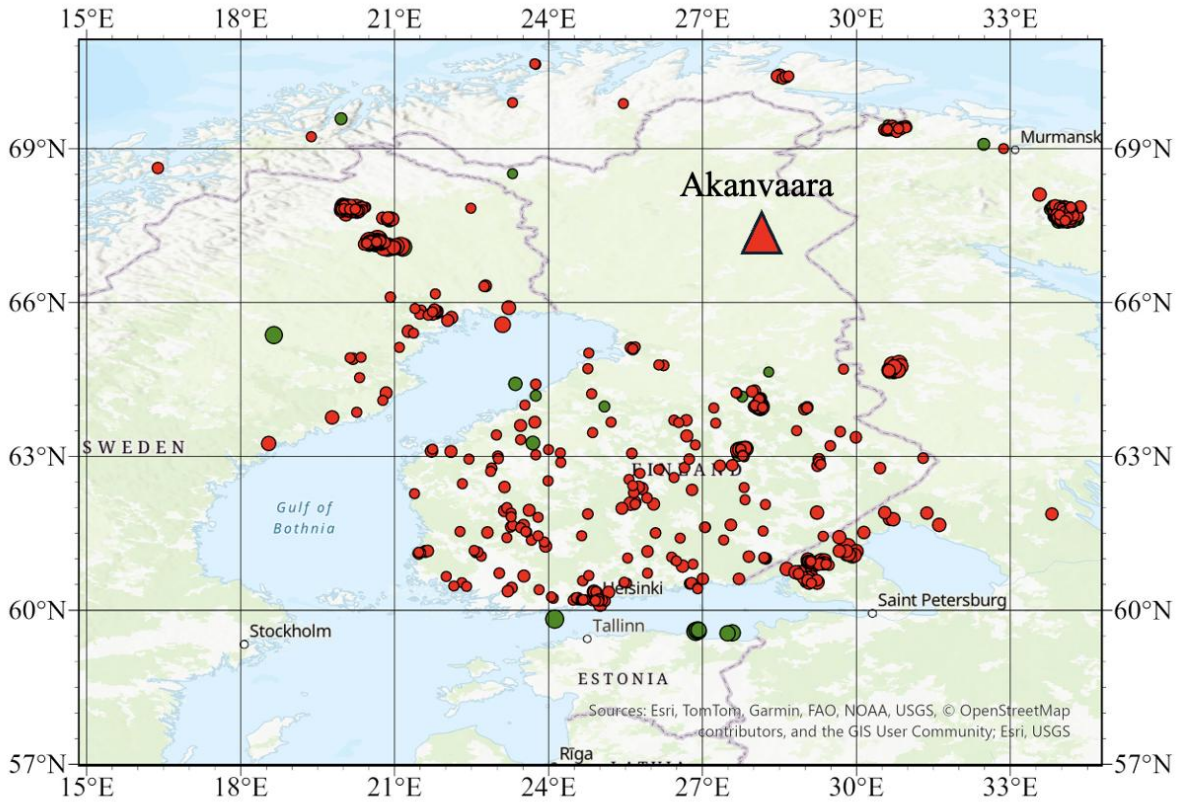



**Fig. 2** Sources of the seismic events, used in the study: green circles used in the first part of the experiment (profile 1 on Fig.1) and red circles in the second part of the experiment (profile 2 on Fig. 1). Sizes of circles are proportional to event magnitude.

During our experiments, several natural local earthquakes with relatively large magnitudes were recorded. An example of seismograms for such an earthquake is shown in Fig. 3. On these seismograms clear Pn and Sn arrivals are seen, as well as some scattered arrivals in their coda, which could be converted waves. Although the Sn coda can be used to evaluate EGT, we used only the Pn coda in our study (blue dashed rectangle in Fig. 3) to avoid possible issues in interpretation caused by the superposition of different waves.

To select proper frequency band for prefiltering the coda before the correlation, we calculated the spectra of all the selected coda signals. To exclude all possible local effects which can distort the results of spectral analysis (e.g. local noise by traffic), we averaged the spectra over all the selected events recorded by each seismometer (Fig. 4.)

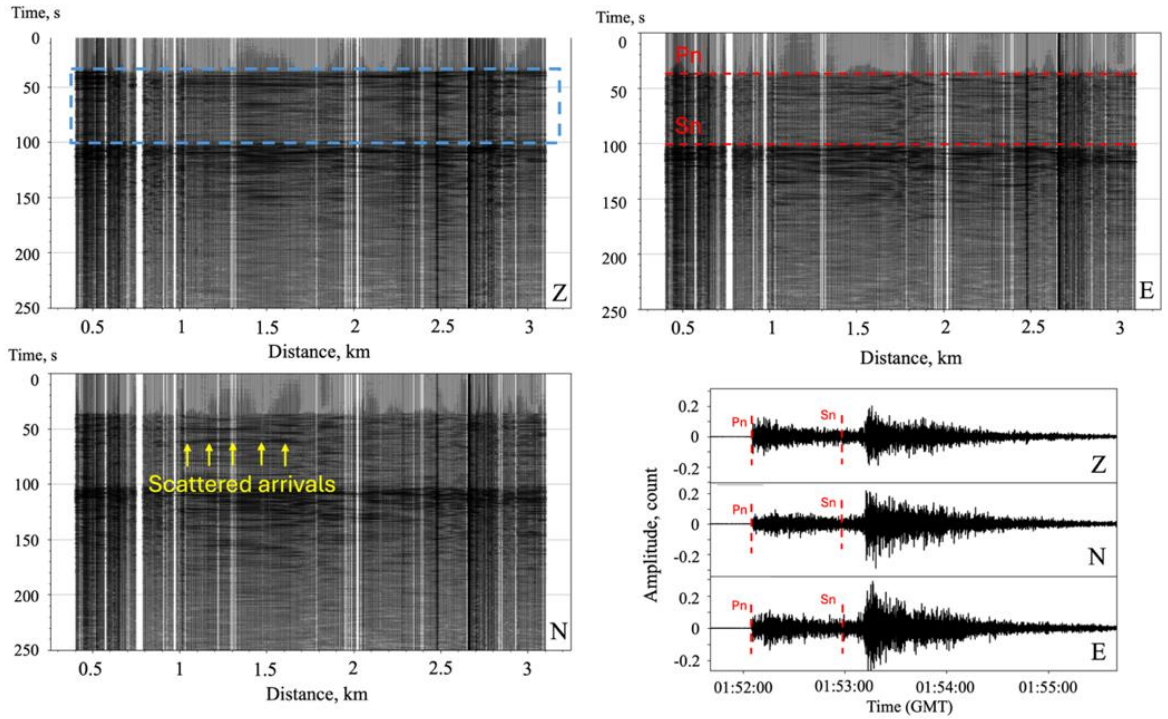



**Fig. 3** On the lower right seismograms of a seismic event on 8.11. 2023 (lat=66.6520N, long=13.3730E Ml=3.1 (Institute of Seismology, University of Helsinki)) and seismic recordings for Z, E and N components for the same event in the profile 1 in Akanvaara. Pn-wave coda contoured by blue dashed rectangle; red dashed lines are Pn and Sn arrivals; yellow arrows are scattered arrivals in Pn-wave coda.

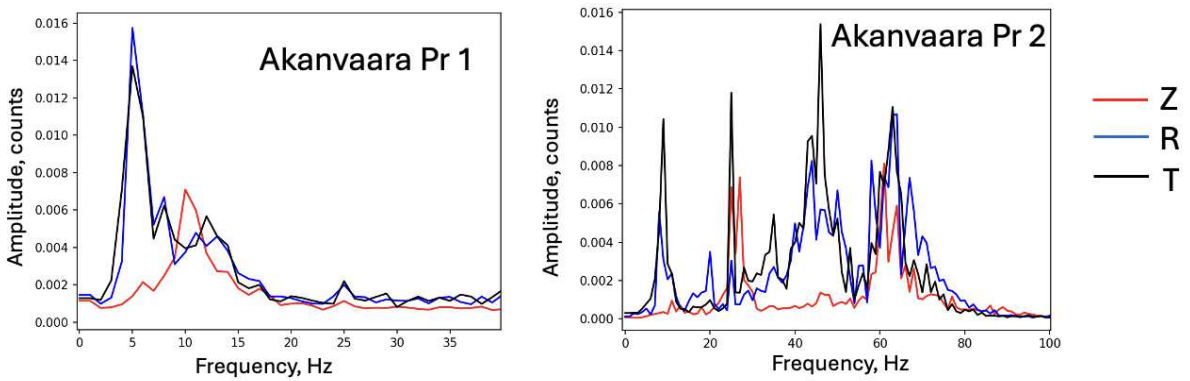



**Fig. 4** Averaged spectra of the Pn-coda for profiles 1 and 2 (Pr1 and Pr2)

All selected Pn-wave codas have a local maxima of amplitudes on vertical components in the frequency range of about 2-15 Hz. Pn-wave codas also have high-frequency signals up to around 80 Hz. These could potentially be used for studying the shallow subsurface down to several tens of meters. The high frequency signals could be

generated by local noise sources, like traffic, as it is known that Pn-waves of regional seismic events in the European Arctic have only low frequencies of about 1.5-10 Hz (Ringdal et al., 2002). Considering that scattered waves in the coda can have frequencies higher than those in the main Pn-wave arrival, we selected a frequency band of 7-12 Hz for our study. A signal with such frequencies and wavelengths is more suitable for our investigation that is interested in depths of few kilometres.

**5. Synthetic experiments**

Numerical simulation was done to demonstrate the origin of the PS and SP converted waves on the structural features of the Akanvaara intrusion and to show that these are detectable on the EGT components obtained by interferometry. The model (Fig. 5) used in the simulation represents a simple inclined layer composed of three major lithologies in the Akanvaara intrusion. The elastic properties were taken from (Lutynski, 2019; Schön, 2015; Dortman, 1994) and presented in Table 1.

Considering the results of spectral analysis of Pn-wave coda (Fig. 4) and statements about Pn-wave coda propagation in previous chapters, we selected plane P- and S-waves frequency of 10 Hz propagating vertically from the bottom of the model to its surface as the initial wavefield in the simulation. The synthetic seismograms were obtained by placing a line of 201 receivers with a spacing of 20 m on the top of the model that represents the ground surface (Fig. 5). The line is located at x from 2000 to 6000 m and z = 4000 m. Synthetic seismograms were calculated with the finite-difference approach described by Virieux (1986) and Levander (1988) and implemented in SOFI3D software (Bohlen, 2002), which was installed in Puhti cluster of CSC - IT Centre for Science of Finland (www.csc.fi). We simulated a three-layer case, with an inclined layer of anorthosite between magnetite gabbro and gabbro. The seismic velocities and densities used are shown in Table 1. Considering that anorthosite layer has thickness of 250 m and its inclination angle can be either 40 or 75 degrees, according to existing geological information (Lutynski, 2019), we simulated both these cases to understand features of plane wave scattering on such structures and impact of inclination angle on origination of converted waves.

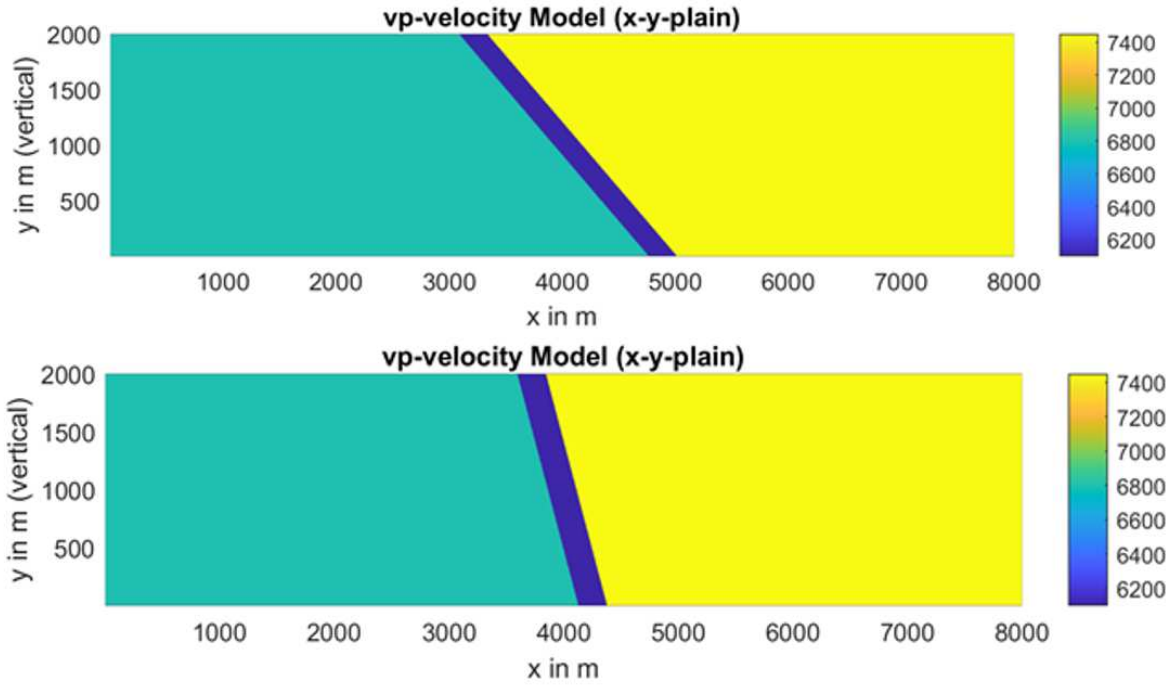



**Fig. 5** The Vp-velocity model used in the synthetic simulation. The following lithologies were used for the model: teal – Gabbro, blue - Anorthosite and yellow - Magnetite gabbro. Y denotes depth of the model

Table 1 – Mechanical properties used in the numerical simulation

| Mechanical properties of layers | | | | | | | | |
|---|---|---|---|---|---|---|---|---|
| Anorthosite | | | Gabbro | | | Magnetite gabbro | | |
| Vp, m/s | Vs, m/s | Rho, kg/m$^3$ | Vp, m/s | Vs, m/s | Rho, kg/m$^3$ | Vp, m/s | Vs, m/s | Rho, kg/m$^3$ |
| 6100 | 3600 | 2680 | 6800 | 4100 | 3000 | 7450 | 4400 | 3500 |

The model dimensions were 8000 m in both horizontal directions and 2000 m in the vertical direction. For the simulations, the model has been discretized to a 1600x400x1600 grid with a cell size of 5 x 5 x 5 m. The plane wave seismic source was at a depth of 1750 m below the surface. The plane waves were simulated by exciting a force from every grid point at the source depth. The P- and S-waves used in the simulation were obtained by using the corresponding direction for the excited force. A perfectly matched layer boundary condition layer of 200 m was added to the sides and bottom of the model, with a free surface boundary condition on top of the model. The output synthetic seismograms have a length of 2 seconds and a sampling period of 0.25 ms.

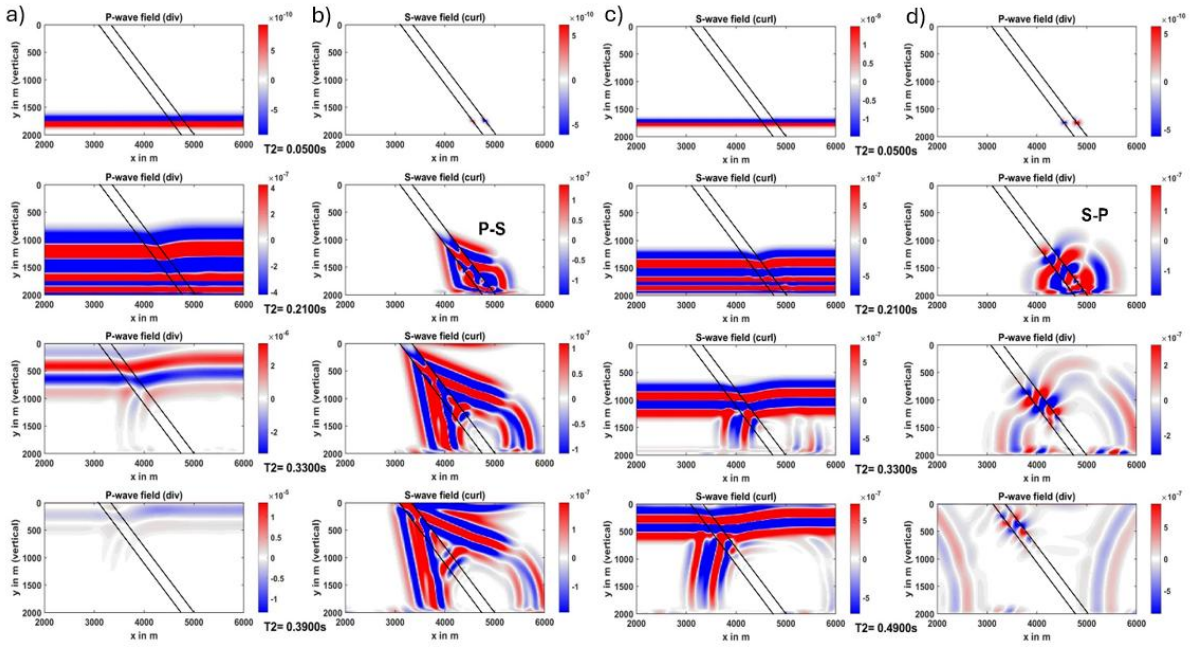



**Fig. 6** The snapshots of P and S wavefields, originated by scattering of P (a, b) and S (c, d) during propagation through the model with 40-degree inclination of the anorthosite layer. T2 is the time from excitation of the plane wave.

On the Figure 6 (a, b) one can see that scattering of P wave on anorthosite layer results in origin of converted PS wave on this layer. This wave arrives on the ground surface with time that is a function of coordinate, and it is proportional to the depth to the layer. Obviously, the depth to this boundary can be calculated using Equation (7) where a time lag should be taken equal to the time lag between the first arrival and arrival time of converted wave. On the Figure 6 (c, d) we show a modelled radial S-wave (Fig. 6, c) that results in S-P conversions at the boundary of the anorthosite layer seen in the corresponding P-wave figures (Fig. 6, d). Nevertheless, the behaviour of scattered wavefield is more complicated in this case. For example, one can see a trapped wave that propagates inside the anorthosite layer. Despite the visible conversion of S to P, the interpretation of SP wave and its arrival times is not so obvious as in case of PS waves, therefore, only rough estimation of the depth to the conversion boundary is possible.

In both cases one can see that part of the plane wave energy is reflecting to the medium and probably being converted to surface wave. Nevertheless, we could not simulate these times, because of limitations of the computational facilities, resulting in limitation on model horizontal sizes. This, in turn, causes artefacts seen on snapshots and seismograms. For example, on the Figure 6 (d) one can notice artefacts, related to reflections from the corners and sites of the models.

In the case when anorthosite layer has inclination angle of 75 degrees (Fig. 7), a significant part of S-wave energy has been converted to trapped wave and less to SP wave (Fig. 7, d). On the Figure 7 (a, b) P-wave arriving from the bottom of the model results in P-S conversions at the boundary of the anorthosite layer (Fig. 7, b). A trapped wave is seen within the anorthosite layer. On the Figure 7 (c, d), for case of scattering a radial S-wave, one can see S to P conversions at the boundary of the anorthosite layer, as well as a trapped wave propagating inside anorthosite (Fig. 7, d). The same artefacts as in previous case are also visible.

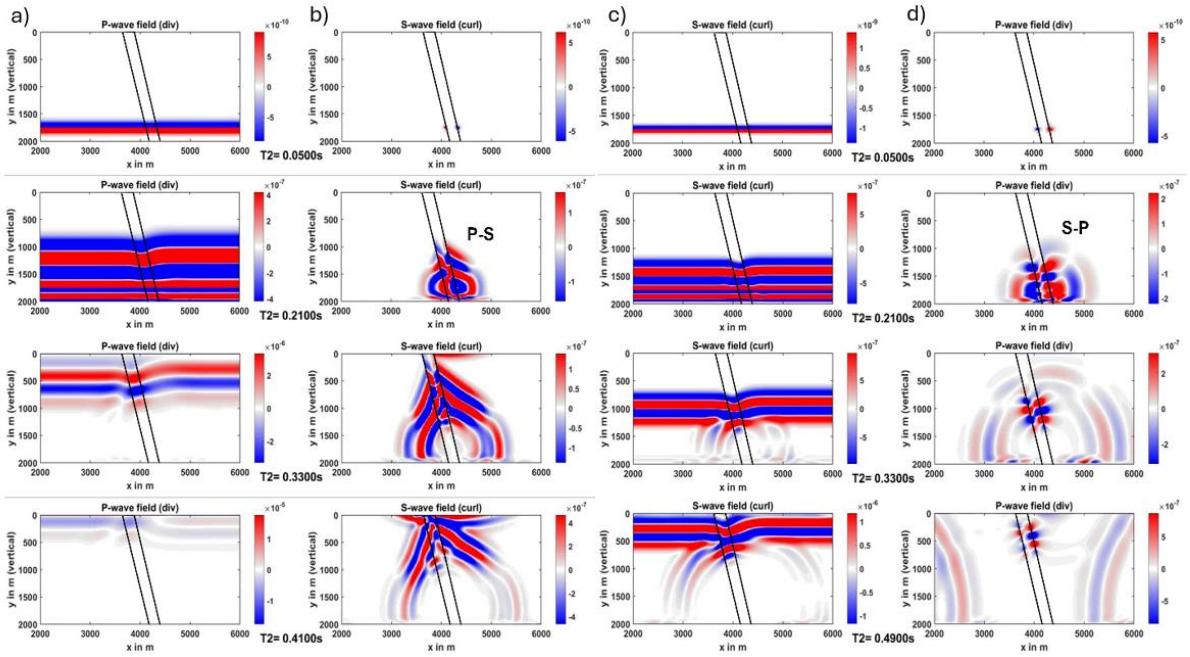



**Fig. 7** The snapshots of P and S wavefields, caused by scattering of P (a, b) and S (c, d) plane waves during propagation through the model with 75-degree inclination of the anorthosite layer. T2 is the time from excitation of the plane wave.

The analysis of snapshots allows to conclude that converted waves originated on the boundary of the anorthosite layer in both cases, therefore, the depths to this layer can be simply calculated from PS arrivals. Interpretation of SP converted and trapped arrivals seems to be more complicated, as they are not very visible in such snapshots as div P and curl S. Unlike snapshots, the SP arrivals are clearly visible on the synthetic seismograms (Fig. 8) on R components in the case of scattering of S-radial wave. A range from 3400m to 4600m was selected for analysis, as structures in this range are located directly above the top of the anorthosite layer. However, the corner artefacts arriving after the P and S and converted waves are also present in this range.

In case of scattering S wave with transverse polarization, the SP arrivals are also visible on transverse components, but their amplitudes are small comparing to those originated when scattering S-wave of radial polarization.

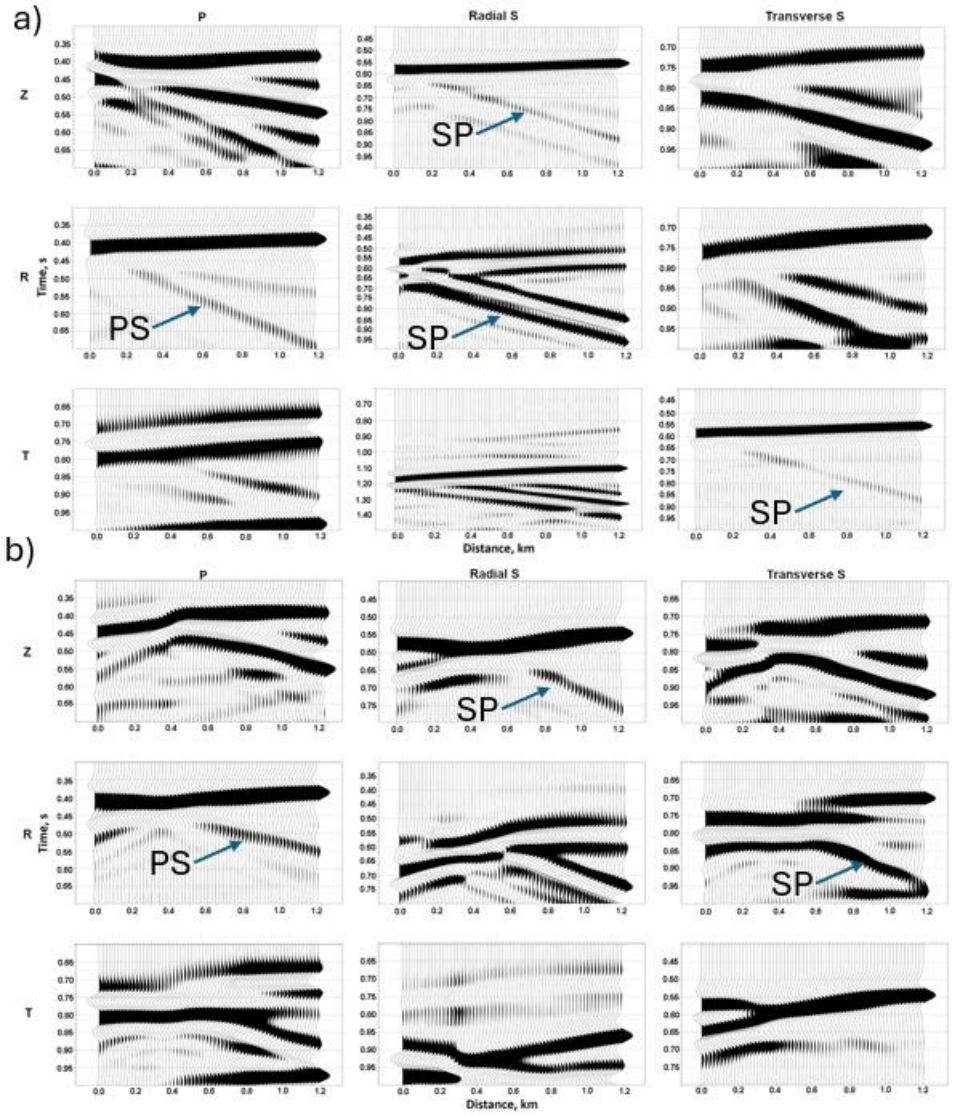



**Fig. 8** Synthetic seismograms for the 40-degree (a) and the 75-degree (b) inclination angle of anorthosite layer. The seismograms were normalized and cut to appropriate lengths for analysis.

Despite on impact of numerous artefacts on synthetic seismograms, the results of synthetic experiments show that converted PS and SP waves should be presented in Pn seismic coda in the case of inclination angle of anorthosite layer either 40 or 75 degrees. Nevertheless, signatures of converted PS and SP waves are visible on both horizontal and vertical components (Fig. 8) what may impact on quality of EGT, obtained by cross-correlation. That is why using of polarization filter is critically important to avoid misinterpretation of arrivals.

**6 Results**

We calculated the correlation functions of the prefiltered Pn coda for every possible channel pair for all stations in the array. For each station, we stacked the calculated correlation functions over all seismic events to obtain the body wave parts of the EGT. Taking into account that in our case we deal with vertically arriving wavefields, we used ZRT coordinate system instead of LQR. Causal parts of the tensor for Profile 1 are shown in Fig. 9 (a) as record sections, in which each trace corresponds to the Green's tensor component for the position of particular seismic sensor. To interpret seismic arrivals seen in the different tensor components, we compared these to the

results of the synthetic modelling (Fig. 8). Modelling suggests that the non-diagonal components of the EGT will mainly show the seismic waves converted at inclined boundaries. At the same time, diagonal components will show signatures of reflected seismic waves.

All the components of the EGT contain arrivals that can be interpreted as reflected arrivals, their multiples or converted arrivals (Fig 9). Some of the components of the tensor (e.g. ZR, ZT) show also clear signatures of the inclined boundaries. To interpret the arrivals and associate them with the lithological boundaries, the uppermost plots show the position of the profile on the geological map, similarly as in Figure 1. The yellow lines indicate possible continuation of the boundaries to the depth, assuming the average dip angle of 45 degrees which is adopted from the drilling data in Akanvaara site. Clear reflected arrivals are visible in the diagonal components ZZ, RR and TT of the EGT, which could be caused by some boundary in the uppermost part of the study area.

Fig. 9 (b) shows the same ZR and ZT components of the EGT, but with the reduced time scale of one second. The objective is to show better correlation between the signatures of the inclined interfaces and position of the geological boundaries.

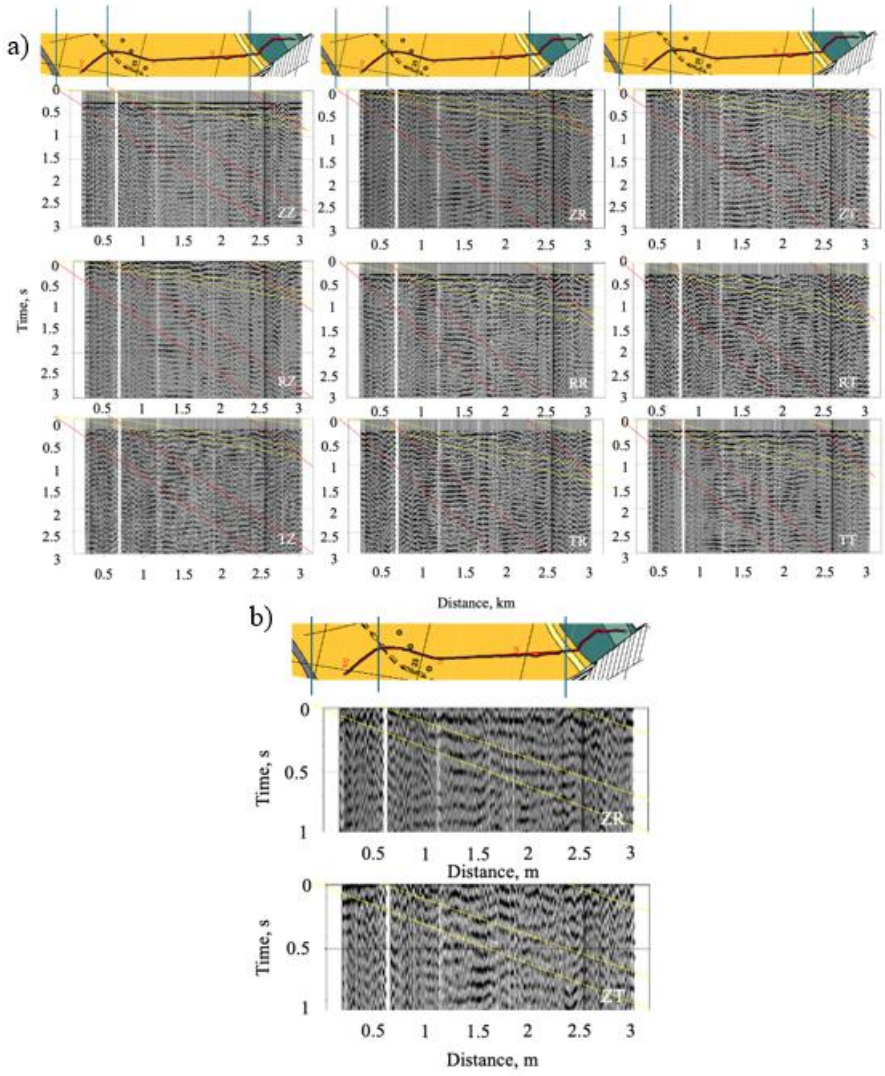



**Fig. 9** a) Empirical Green's tensors and respective geological map along Profile 1. Yellow dotted lines indicate continuation of boundaries between lithological units with dip angle of 45 degrees, red dotted lines indicate

continuation of the boundaries, with larger dip angle (75 deg.); b) ZR and ZT component of the EGT with reduced time axis.

In Fig. 9b arrivals correlating with three different dipping boundaries can be identified. These correlate well with the: 1) contact of mineralised pyroxene cumulate with gabbro; 2) UC thin chromitite embedded in gabbro 3) contact of anortosites with gabbro and magnetite gabbro. However, it is also seen that the dip of pyroxene-gabbro boundary is larger than the assumed 45 degrees dip. The dip could be as high as 70 degees, and the boundary can be traced up to 2.5 seconds in ZR and ZT components.

The seismograms of EGT for Profile 2 are shown in Figure 10. On these EGT one can see arrivals of reflected and converted waves, that correlate with lithological units on geological map. However, their interpretation is quite difficult because of long coda of arrivals.

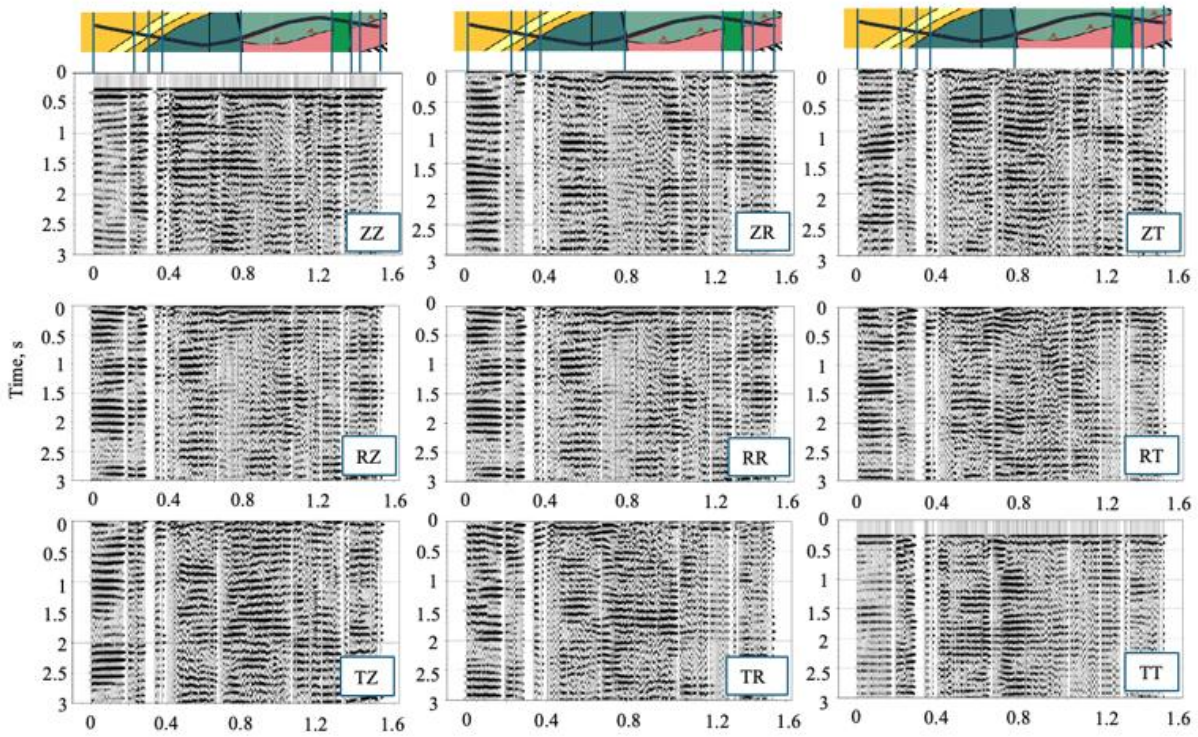



**Fig. 10** Empirical Green's tensors, evaluated from seismic records of profile 2.

To improve visualization of arrivals seen in Profile 2, we picked all arrivals by maxima on EGTs and plotted them together in one plot (Fig.11), depending on wave type (reflected P, reflected S, converted PS and SP). Such visualization is similar to so-called "line-drawing" that has been widely used in reflection seismic data processing and visualisation. To calculate depths, we used seismic velocities from Table 1 and Eq. 7 (for converted arrivals). Generally, the P and S images show more clearly the features corresponding to horizontal and sub-horizontal boundaries, while the SP and PS images show several inclined boundaries not visible in S- and P- images.

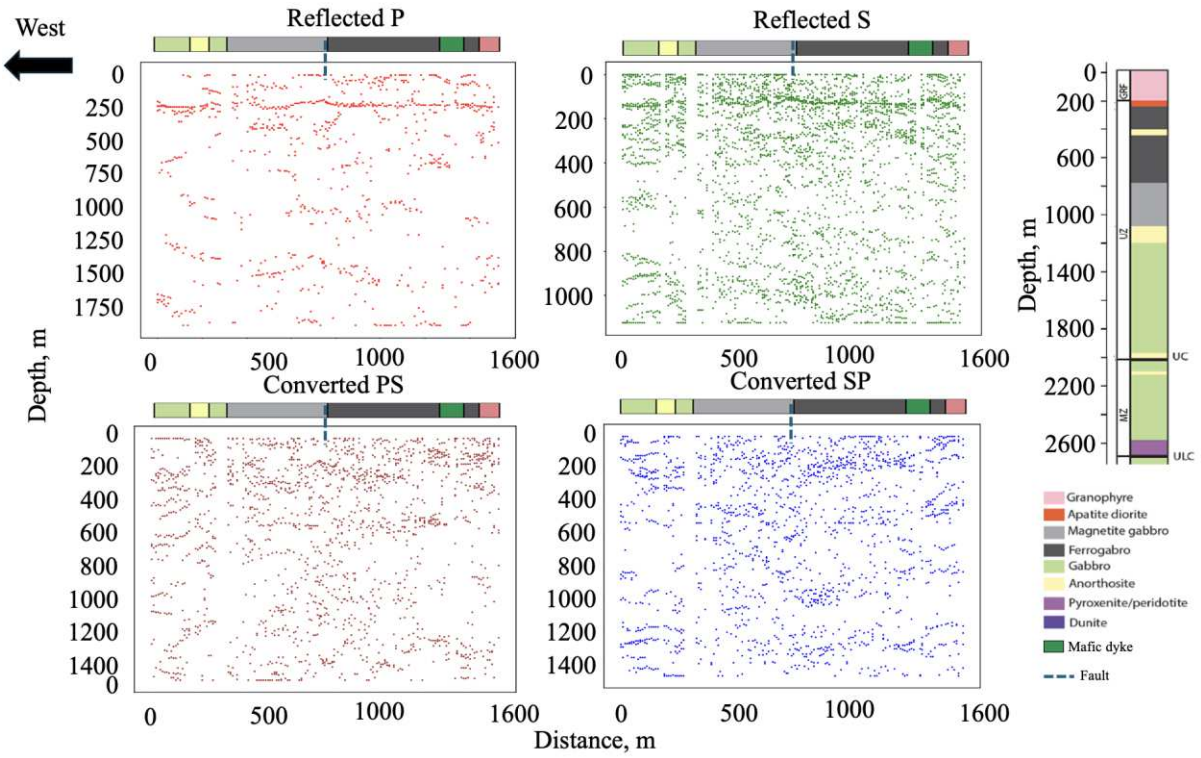



**Fig. 11** Picked arrivals on EGT (profile 2). Horizontal color bar shows the geological units according to geological map (Fig. 1). Vertical bar – drillhole data

We compared these plots with the geological model compiled from drillhole data (vertical bar on the plot) and data from the geological map (Fig. 1) (horizontal bars above sections). On depths of 200-250 m one can see reflections of P and S waves from some sub-horizontal boundary. According to drillhole data, the boundary on this depth may separate granophyre, apatite diorite and ferrogabro. However, these lithologies were not present in the area of Profiles 1 and 2, so the more plausible explanation is that this is the lower boundary of uppermost fractured layer. The same boundary is clearly visible on diagonal components of EGT of Profile 1 (Fig. 12). On Profile 2, the reflected arrivals of P and S waves on depths of about 200-250 m are also visible at all distances. This is additional evidence in support of explanation that these reflected waves might originate on the same lower boundary of fractured uppermost layer. Noticeable that on distances from 0 to 800 m of Profile 2 (Fig. 11), the boundaries indicated by converted SP arrivals are dipping to the East, while on distances from 800 to 1600 m, these boundaries are dipping in the opposite direction. According to the geological map (Fig. 1), the middle part of the profile corresponds to the contact zone (fault), along which two geological blocks were probably moved. Between distances of 800 and 1600 m in Profile 2, one can see arrivals of the SP waves from a boundary dipping to the west from 0 to 200 m. This boundary may separate either a mafic dyke or a granophyre and ferrogabro. Fragments of sub-horizontal reflection boundaries at a depth of 400 m and 600 m are seen in both P and S wave images. According to the geological map, they could correspond to the thin layers of anorthosite within ferrogabro. Reflected arrivals of S waves are seen at depths of 400 and 600 m at distances between about 700 and 1400 m (Fig. 12 a). These reflected waves could originate in thin anorthosite layers and the boundaries that separate magnetite gabbro and ferrogabro. At distances of about 1500 m (Fig. 12 a), one can see a reflector in P-wave image near the surface dipping to the north. At the same distances and with the same dipping direction, a reflector

in S-wave image is observed. Both these reflectors can correspond to a fault plane. At a distance of about 700 m (Fig. 12 a), one can see the step in depth of the S-wave reflector at a depth of about 200 m. It can be due to a fault zone that could be related to UC chromitite mineralisation according to the geological map.

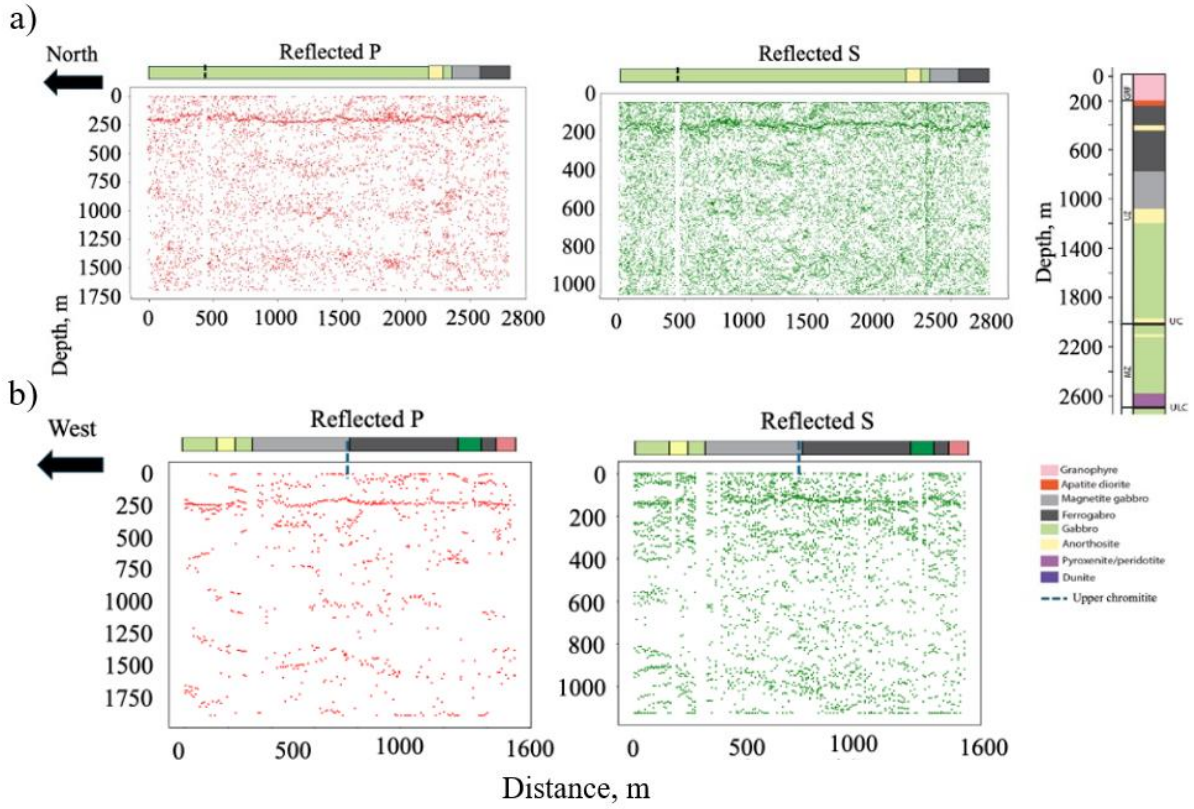



**Fig. 12** Reflected P and S arrivals, detected on diagonal EGT components: a) Profile 1; b) Profile 2.

**7 Discussion and conclusions**

Despite numerous applications of ground-based near-vertical reflection seismics in exploration and mining planning in hard rock terrains, detection of steeply dipping boundaries associated with mineralisation remains a challenge, even with the 3-D acquisition geometry (Kukkonen et al., 2011; Malehmir et al. 2012a; Cheradi et al., 2012). However, such boundaries are routinely detected in VSP measurements, which have different position of incoming wavefront with respect to target (Bellefleur et al., 2004; Malehmir et al., 2012b). Numerical simulation of wavefield from controlled sources using finite-difference methods predicts that dipping boundaries or ore bodies with contrasting elastic properties produce wavefield that is dominated by shear-wave events and contain converted waves (Bohlen et al., 2003; Bellefleur et al., 2012) that are detected better from three component seismic data.

In this study, we try to solve the problem of detecting steeply dipping boundaries using passive seismic methods, in which we used Pn codas of regional seismic events (earthquakes and mining blasts). We utilized the theoretical background and principles of the receiver function method, teleseismic coda wave interferometry and autocorrelation of teleseismic P-wave coda. By merging the above-mentioned techniques and utilising the results of numerical simulations conducted in this study, we developed a new passive seismic method that can be applied to study the inner structure of ore deposits, in which steeply inclined boundaries are often observed.

The previously done modelling was mainly related to investigating the scattering of the wavefield of the controlled seismic sources in massive sulphide deposits (Bohlen et al., 2003; Bellefleur et al., 2012), while our numerical modelling aimed to investigate the scattered wavefield in the orthomagmatic mineral deposits in layered mafic intrusion, in which differently compositional strata formed due to rise of magmas along pre-existing vertical and sub-vertical sutures and faults. The Akanvaara intrusion is one typical example of such intrusions that are videly spread in Fennoscandia. As different strata inside such intrusions often host important economically significant minerals, the methods capable to map their inner structure are relevant. Our modelling shows that converted waves generated by scattering of a plane-wave on the inner boundaries inside ultramafic layered intrusion can be identified in 3-component recordings and utilized for the purpose of detection of steeply dipping boundaries that are not easily detectable in conventional controlled-source seismic experiments. We showed that converted PS and SP arrivals could be retrieved from the body wave part of the empirical Green's tensor using cross-correlation of a Pn-wave coda of regional seismic events recorded in the high-resolution passive seismic profile.

We tested our method with the seismic data recorded during a high-resolution passive seismic experiment in the Akanvaara layered intrusion in northern Finland. With this method we obtained important information about the inner structure of the intrusion, namely, we detected several conversion boundaries and reflectors that corresponds to: 1) contact of mineralised pyroxene cumulate with gabbro; 2) UC thin chromitite embedded in gabbro 3) contact of anortosites with gabbro and magnetite gabbro. Moreover, it is also seen that the dip of pyroxene-gabbro boundary is larger than the assumed 45 degrees deeper. This dip could be as high as 70 degees, and the boundary can be down to 1000-1200 m.

Generally, it could be concluded that the method, presented in this study is a promising exploration method that can be used as an effective and environmentally friendly tool for brownfield exploration of orthomagmatic mineral deposits, in which mineralised bodies often lack clear electromagnetic response.

**Author contribution:** NA: conceptualization of the research, planning and conducting the passive seismic experiments, software development, data processing, interpretation of the results, the manuscript preparation; EK: conceptualization and supervision of the research, interpretation of the results, the manuscript preparation; KM: planning organizing and conducting passive seismic experiments. Took part in the manuscript preparation; SY: PI of the SEMACRET project. Took part in the interpretation of the results and the manuscript preparation; JS: the numerical simulation and the manuscript preparation.

**Competing interests:** The authors declare that they have no conflict of interest

**Acknowledgements**

This work is a part of the SEMACRET project: ("Sustainable exploration for orthomagmatic (critical) raw materials in the EU: Charting the road to the green energy transition"). The authors wish to thank CSC - IT Center for Science, Finland (urn: nbn:fi: research-infras-2016072531) and the Open Geospatial Information Infrastructure for Research (Geoportti, urn: nbn:fi: research-infras-2016072513) for computational resources and support.

**Reference**

Afonin, N., Kozlovskaya, E., Nevalainen, J., & Narkilahti, J. (2019). Improving the quality of empirical Green's functions, obtained by cross-correlation of high-frequency ambient seismic noise. *Solid Earth*, 10(5), 1621-1634.

Afonin, N., Kozlovskaya, E., Heinonen, S., & Buske, S. (2021). Near-surface structure of the Sodankylä area in Finland, obtained by passive seismic interferometry. *Solid Earth*, *12*(7), 1563-1579.

Afonin, N., Kozlovskaya, E., & Canales, R. M. (2022). Application of passive seismic interferometry for mapping mining waste storage facilities: A case study of Pyhäsalmi mine in Finland. *Journal of Applied Geophysics*, 202, 104669.

Afonin, N. (2022). *Development of passive seismic interferometry to study shallow subsurface structure*. PhD thesis.

Aki, K., & Richards, P.G. (2002). *Quantitative Seismology. 2nd Edition*, CA: Univ. Sci. Books, Sausalito.

Bellefleur, G., Müller, C., Snyder, D., & Matthews, L. (2004). Downhole seismic imaging of a massive sulfide orebody with mode-converted waves, Halfmile Lake, New Brunswick, Canada. *Geophysics*, *69*(2), 318-329.

Bellefleur, G., Malehmir, A., & Müller, C. (2012). Elastic finite-difference modeling of volcanic-hosted massive sulfide deposits: A case study from Half Mile Lake, New Brunswick, Canada. *Geophysics*, *77*(5), WC25-WC36.

Beylkin, G., & Burridge, R. (1990). Linearized inverse scattering problems in acoustics and elasticity. *Wave motion*, 12(1), 15-52.

Bohlen, T., Miller, C., & Milkereit, B. (2003). *Hardrock Seismic Exploration*. Society of Exploration Geophysicis.

Bostock, M. G. (2004). Green's functions, source signatures, and the normalization of teleseismic wave fields. *Journal of Geophysical Research: Solid Earth*, *109*(B3).

Brinkman, N., Sollberger, D., Schmelzbach, C., Stähler, S. C., & Robertsson, J. (2023). Applications of time-frequency domain polarization filtering to insight seismic data. *Earth and Space Science*, 10(11), e2023EA003169.

Campillo, M., & Paul, A. (2008). *Long-range correlations in the diffuse seismic coda.*

Cheraghi, S., Malehmir, A., & Bellefleur, G. (2012). 3D imaging challenges in steeply dipping mining structures: New lights on acquisition geometry and processing from the Brunswick no. 6 seismic data, Canada. *Geophysics*, *77*(5), WC109-WC122.

Draganov, D., Campman, X., Thorbecke, J., Verdel, A., & Wapenaar, K. (2009). Reflection images from ambient seismic noise. *Geophysics*, 74, A63–A67.

Flinn, E. A. (1965). Signal analysis using rectilinearity and direction of particle motion. *Proceedings of the IEEE*, *53*(12), 1874-1876.

Greenhalgh, S., Zhou, B., & Cao, S. (2003). A crosswell seismic experiment for nickel sulphide exploration. *Journal of Applied Geophysics*, 53, 77–89.

Janik, T., Kozlovskaya, E., & Yliniemi, J. (2007). Crust-mantle boundary in the central Fennoscandian shield: Constraints from wide-angle P and S wave velocity models and new results of reflection profiling in Finland. *Journal of Geophysical Research: Solid Earth*, *112*(B4).

Janik, T., Kozlovskaya, E., Heikkinen, P., Yliniemi, J., & Silvennoinen, H. (2009). Evidence for preservation of crustal root beneath the Proterozoic Lapland-Kola orogen (northern Fennoscandian shield) derived from P and S wave velocity models of POLAR and HUKKA wide-angle reflection and refraction profiles and FIRE4 reflection transect. *Journal of Geophysical Research: Solid Earth*, *114*(B6).

Jurkevics, A. (1988). Polarization analysis of three-component array data. *Bulletin of the seismological society of America*, *78*(5), 1725-1743.

Hanski, E., Walker, R. J., Huhma, H., & Suominen, I. (2001). The Os and Nd isotopic systematics of c. 2.44 Ga Akanvaara and Koitelainen mafic layered intrusions in northern Finland. *Precambrian Research*, *109*(1-2), 73-102.

Hillers, G., Koivisto, E., Haapanala, P., Kukkonen, I., Courbis, R., Ding, Y., ... & Tiira, T. (2025). FINNSIP-The mobile Finnish Seismic Instrument Pool. *Seismica*, *4*(1).

Schuster, G. T. (2008). *Theory of daylight/interferometric imaging: tutorial.*

Kukkonen, I. T., Laitinen, J., Heikkinen, P., Heinonen, S., Nurmi, P. A., Kousa, J., ... & Moissa, I. (2011). Reflection seismics in exploration for mineral deposits: Initial results from the HIRE project. *Special Paper of the Geological Survey of Finland*, *2011*(49), 49-58.

Lobkis, O. I., & Weaver, R. L. (2008). *On the emergence of the Green's function in the correlations of a diffuse field.*

Lutynski, P. (2019). Akanvaara project, Tech. rep., Finland: Technical report. *Strategic Resources Inc.,* 49 pp

Malehmir, A., Durrheim, R., Bellefleur, G., Urosevic, M., Juhlin, C., White, D. J., Milkereit, B., & Campbell, G. (2012). Seismic methods in mineral exploration and mine planning: A general overview of past and present case histories and a look into the future. *Geophysics*, 77, 285 WC173–WC190.

Malehmir, A., Juhlin, C., Wijns, C., Urosevic, M., Valasti, P., & Koivisto, E. (2012). 3D reflection seismic imaging for open-pit mine planning and deep exploration in the Kevitsa Ni-Cu-PGE deposit, northern Finland. *Geophysics*, *77*(5), WC95-WC108.

Mutanen, T. (1997). *Geology and ore petrology of the Akanvaara and Koitelainen mafic layered intrusions and the Keivitsa-Satovaara layered complex, northern Finland* (Vol. 395). Geological Survey of Finland.

Mutanen, T. (2005). *Field trip guidebook: The Akanvaara intrusion and the Keivitsa-Satovaara Complex, with stops at Kaikkivaltiaanlehto and Rantavaara intrusions* (Vol. 51). Geological Survey of Finland.

Oren, C., & Nowack, R. L. (2016). Seismic body-wave interferometry using noise auto-correlations for crustal structure. *Geophysical Journal International*, p. ggw394.

Nguyen, D. T., Brown, R. J., & Lawton, D. C. (1989). Polarization filter for multi-component seismic data. *CREWES Research Report*, *7*, 93-101.

Pavlis, G. L. (2005). Direct imaging of the coda of teleseismic P waves. *GEOPHYSICAL MONOGRAPH-AMERICAN GEOPHYSICAL UNION*, *157*, 171.

Poli, P., Pedersen, H., Campillo, M., & Group, P. W. (2013). Noise directivity and group velocity tomography in a region with small velocity contrasts: The northern Baltic shield. *Geophysical Journal International,* 192, 413–424.

Ringdal, F., Kremenetskaya, E., & Asming, V. (2002). Observed characteristics of regional seismic phases and implications for P/S discrimination in the European Arctic. *pure and applied geophysics*, *159*(4), 701-719.

Scherbaum, F. (1987). Seismic imaging of the site response using microearthquake recordings. Part I. Method. *Bulletin of the Seismological Society of America*, *77*(6), 1905-1923.

Schuster, G. T. (2008). *Theory of daylight/interferometric imaging: tutorial*.

Snieder, R. (2006). The theory of coda wave interferometry. *Pure and Applied geophysics*, *163*(2), 455-473.

Stolt, R. H., & Weglein, A. B. (1985). Migration and inversion of seismic data. *Geophysics*, 50(12), 2458-2472.

Sun, R., Li, J., Yan, Y., Liu, H., Bai, L., & Chen, Y. (2024). Three-dimensional urban subsurface space tomography with dense ambient noise seismic array. *Surveys in Geophysics*, 45(3), 819-843.

The European Commission (2023). *European Critical Raw Materials Act*. Retrieved September 24, 2024 from https://ec.europa.eu/commission/presscorner/detail/en/ip_23_1661.

Tiira, T., Janik, T., Kozlovskaya, E., Grad, M., Korja, A., Komminaho, K., ... & BrŰckl, E. (2014). Crustal architecture of the inverted Central Lapland Rift along the HUKKA 2007 profile. *Pure and Applied Geophysics*, *171*(7), 1129-1152.

Vidale, J. E. (1986). Complex polarization analysis of particle motion. *Bulletin of the Seismological society of America*, *76*(5), 1393-1405.

Vinnik, L. (1977). Detection of waves converted from P to SV in the mantle. *Physics of the Earth and planetary interiors*, 15, 39–45.

Vinnik, L. P. (2019). Receiver function seismology. *Izvestiya, Physics of the Solid Earth*, *55*(1), 12-21.

Wang, C., Tauzin, B., Pham, T. S., & Tkalčić, H. (2020). On the efficiency of P-Wave coda autocorrelation in recovering crustal structure: examples from dense arrays in the Eastern United States. *Journal of Geophysical Research: Solid Earth*, *125*(12), e2020JB020270.

Weglein, A. B., Gasparotto, F. A., Carvalho, P. M., & Stolt, R. H. (1997). An inverse-scattering series method for attenuating multiples in seismic reflection data. Geophysics, 62(6), 1975-1989.

Wu, R. S., & Aki, K. (1985). Scattering characteristics of elastic waves by an elastic heterogeneity. Geophysics, 50(4), 582-595.

Weaver, R. L. (1982). On diffuse waves in solid media. *Journal of the Acoustical Society of America*, 71(6), 1608-1609.

Zhang, Y., Li, Y. E., Zhang, H., & Ku, T. (2019). Near-surface site investigation by seismic interferometry using urban traffic noise in Singapore. *Geophysics*, 84(2), B169-B180.

Zhu, L., & Kanamori, H. (2000). Moho depth variation in southern California from teleseismic receiver functions. *Journal of Geophysical Research: Solid Earth*, *105*(B2), 2969-2980.

Yang, J., & Shragge, J. (2023). Long-term ambient seismic interferometry for constraining seasonal subsurface velocity variations in urban settings: a distributed acoustic sensing (DAS) case study. *Geophysical Journal International*, 234(3), 1973-1984.